Pilot investigation of surface-tilt and gas amplification induced contrast during electronic imaging for potential *in-situ* electron beam melting monitoring

Author: Hay Wong[a]

[a]School of Engineering, University of Liverpool, The Quadrangle, Brownlow Hill, United Kingdom L69 3GH

Corresponding author's email: Hay Wong – hay.wong@liv.ac.uk

Keywords: Electron beam melting; *in-situ* monitoring; electronic imaging; surface-tilt contrast; gas amplification

Abstract

Electron Beam Melting (EBM) is a powder bed fusion (metal additive manufacturing) technique employed by many industrial sectors. *In-situ* EBM monitoring for quality assurance purposes has been a popular research area, and the potential of electronic imaging has been investigated recently. The imaging conditions inside an EBM machine are different from that of a typical scanning electron microscope. These differences are thought to affect image quality, and investigations should be carried out to understand the potential challenges of carrying out electronic imaging inside an EBM machine. This study addresses two of these challenges: (1) surface-tilt image contrast due to large-area imaging, and (2) gas amplification of the feedback electron signal due to the presence of chamber gas. This knowledge gap was tackled by the following approach: (1) estimating both the feedback electron yield and gas amplification of electron signal during electronic imaging; (2) simulating the surface-tilt image contrast during large-area imaging; and (3) presenting an electronic imaging experiment conducted at room temperature to investigate the influence of surface-tilt and gas amplification on image contrast. Experimental results indicate that when conducting electronic imaging in a typical EBM machine, the total feedback electron yield is of the order of 20%; the surface-tilt image contrast is insignificant over the EBM machine processing area; and the influence of gas amplification creates observable, non-uniform signal variation when imaging was conducted over a plain stainless steel plate. This article serves as a pilot study, laying the scientific foundation for subsequent investigations into

another challenge under real EBM condition, i.e. the influence of metallisation during melt-pool electronic imaging.

1. Introduction

1.1 The need for EBM process monitoring

Electron Beam Melting (EBM) is a powder bed fusion process, one of the metal Additive Manufacturing (AM) techniques, which makes use of an accelerated electron beam as the energy source to melt metallic powder in a layer-by-layer fashion, forming components based on the geometry of the imported three dimensional (3D) Computer Aided Design (CAD) model [1]. The EBM process allows a reduction in the residual stress within components [2], and offers a high level of design freedom [3]. This technique shows great promise in the manufacture of orthopaedic implants and aerospace components [4]. Nevertheless, the EBM process is prone to quality issues and component defects. They include: non-uniform powder layer deposition [5], peeled-off metallisation falling onto the processing area [6], and component defects including, material porosity [5], balling along melt tracks [7], and delamination of the processed EBM layers [8]. The wider uptake of EBM in industry is hindered unless an effective EBM process monitoring and validation system is available for *in-situ* monitoring [9]. Until recently, EBM layer-quality monitoring has mainly involved the application of thermal/ optical imaging systems [10-13]. In 2018-19, the potential of electronic imaging for monitoring purposes has also been demonstrated [14, 15].

1.2 Addressing the research gap of conducting electronic imaging inside an EBM machine

A commercial Arcam A1 EBM machine, hereinafter referred to as "the EBM machine", is used in this study. Table 1 summarises the key differences between the EBM machine [16] and a typical Scanning Electron Microscope (SEM) and Low-Vacuum SEM (LVSEM). Despite LVSEM and SEM have been studied extensively, differences in the EBM machine hardware and EBM condition nevertheless pose unique challenges for electronic imaging. These challenges include: (1) surface-tilt image contrast due to large-area imaging at temperatures within typical EBM range, (2) gas amplification of the feedback electron signal due to the presence of chamber gas at temperatures within typical EBM range, and (3) metallisation condensing onto electron sensors when melt-pool imaging is conducted under real EBM building condition.

With regard to the influence of temperature on electronic imaging, both theoretical prediction [17] and experimental observation [18] have shown that temperature has little to no effect on the feedback electron signal. The theoretical argument is premised on the ratio between the scale factor of the kinetic energy of an atom, kT (where k is the Boltzmann'sconstant), to the average SE or BSE energy [17]. By convention, the minimum energy of a SE and BSE are 2 eV and 50 eV [19] whereas the primary electron in an EBM machine has an energy of 60 keV [16]. Typical EBM melt-pool temperature is of the order of 1500°C [20,21]. At 1500°C, kT has a value of approximately 0.15 eV, which is only 7.5% of the least energetic SE. SE and BSE are generated from interactions between a primary electron beam and its target atoms [22]. Therefore, at 1500°C the thermal vibration of atoms in the target, which is proportional to the kinetic energy kT, is not expected to affect the yield of either SE or BSE. Experimental finding supports this theoretical prediction by showing that there is no observable reduction in image quality at a range of elevated temperatures (from room temperature to 650 ± 10 °C) [18].

As temperature, within the typical EBM operating range, has little to no effect on electronic imaging, this study therefore was set out to: (1) decouple the influence of metallisation during melt-pool imaging from that of surface-tilt and gas amplification, and (2) reduce the complexity of carrying out multi-layer electronic imaging under real EBM condition. This pilot study intended to conduct single-layer electronic imaging at room temperature on a plain target, i.e. with minimal observable features/ patterns, therefore not to mask the potential image contrast induced by surface-tilt/ gas amplification. Findings from this study shall advise subsequent trials when the investigation is extended to include real-time melt-pool imaging under real EBM building condition.

Table 1 Major differences in hardware and operating condition between an Arcam A1 EBM machine and a typical SEM

Aspect	Typical in EBM machine	Typical in SEM
Accelerating voltage (kV)	60 [16]	1-50 [23]
Imaging target/ sample temperature (°C)	> 1200 (melt-pool imaging) [20, 21] 700 (post-melt imaging) [24]	-25 to +160 [23]
Main complication during imaging	Metallisation/ metal vapour formation (melt-pool imaging) [6] Local fluctuation in feedback electron signal due to vacuum level [25], surface-tilt contrast [26] and large-area imaging (post-melt imaging)	Sample heating [27]
Maximum imaging target area (mm x mm)	200 x 200 [2]	32 x 32 [28] (assuming square stage)
Working distance (mm)	400 ± 10 [24]	10 to 38 [29]
Chamber vacuum level (mbar)	2×10^{-3} [2]	$< 1 \times 10^{-5}$ [30] $> 1 \times 10^{-1}$ (LVSEM) [30]

2. Materials and Methods

Both theoretical analysis and experimental investigation were conducted in this study. Analysis provided scientific understanding whilst experiment validated the theory with first-hand data collected inside a commercial EBM machine. This article first presents the estimation of gas amplification of electron signal. This will be followed by the estimation of Secondary Electrons (SE) yield and Backscattered Electrons (BSE) coefficient when imaging is conducted inside the EBM machine. Surface-tilt contrast simulation will be presented next with SE and BSE yields being used as simulation inputs. Finally, the electronic imaging experimental setup will be described. In this study, a stainless steel plate was chosen to serve as an imaging target owing to the simplicity of the setup. The element iron was used to represent 316L stainless steel in analyses and simulations conducted in this study.

2.1 Estimation of gas amplification of electron signal

The presence of gas leads to feedback electrons-gas ionisation events. The ionised, liberated electrons give rise to background noise as these electrons do not contain direct information from the imaging target material [28]. Eq. 1 [29] defines the extent of the undesired gas amplification of the feedback electrons signal. In one of their work about the ionisation of helium, Ran et al estimated the first Townsend's ionisation coefficient of helium in Fig. 6 of their article [25]. Table 2 summarises the estimation of undesired gas amplification in the EBM machine.

$$\frac{I_{amp}}{I_{Feedback}} = e^{\alpha_{ion} L_{W.D}}$$

$$G_{amp} = e^{\alpha_{ion} L_{W.D}} \tag{1}$$

Where

I_{amp} (mA) is the gas-amplified feedback electron signal, $I_{Feedback}$ (mA) is the total feedback electron signal (SE and BSE) from a target material in the absence of gas, G_{amp} is the gain, α_{ion} (mm^{-1}) is the first Townsend ionisation coefficient of a gas, and $L_{W.D}$ (mm) is the working distance

A typical SEM electron sensor has a bias electric potential applied to it to attract feedback electrons [29]. In this study, no bias potentials were applied to the custom-built electron sensor used. As a result, when referring to Fig. 6 in the article by Ran et al [25], the electric field involved in this study is set to zero in this estimation, and the α/P_0 ratio with a value of

1.5 is chosen as an estimated data point to represent the condition used in this study. Table 2 summarises the estimation result.

Table 2 Gas amplfication estimation

Parameter	Value
E (V cm^{-1})	0
$L_{W.D}$ (mm)	400
P_0 (mbar)	2.00×10^{-3}
α_{ion}/P_0 (10^{-2}cm^{-1} mmHg^{-1})	1.50
α_{ion}/P_0 (mm^{-1}mbar^{-1})	0.0113
G_{amp}	1.01

Table 2 shows that the gas amplification ratio is estimated to be 1.01, thus the noise signal level induced by electron-gas ionisation events is expected to be of the order of 1 % of the total feedback electron signal strength (SE and BSE).

2.2 BSE coefficient estimation

In two studies regarding BSE coefficient and SE yield, Reimer et al [31] and Miller et al [32] presented their BSE coefficient measurements in Fig. 4 [31] and Fig. 18 [32] respectively. BSE coefficient is the ratio of BSE current to the primary electron current. These measurements were obtained at various primary electron beam energy ranges, with the beam incident angle at 0° (the beam is perpendicular to the imaging target surface). Fig. 4 in the article by Reimer et al [31] shows that when the beam energy exceeds 10-30 kiloelectronvolts (keVs), the BSE coefficient can be regarded as independent of the beam energy (thus independent of accelerating voltage), whilst elements with greater atomic number (Z) lead to greater BSE coefficients. Therefore, it is estimated that when imaging iron (Z = 26) at 60 keV, the BSE coefficient would be between 0.2 (Si, Z = 14) and 0.3 (Cu, Z = 29). Fig. 18 in the article by Miller et al [32] shows that when the beam energy is in the megaelectronvolts (MeVs) range, BSE coefficient decreases when the energy of the primary electron beam

increases. When imaging iron at 60 keV, the same BSE coefficient which is in the range of 0.2 to 0.3 is estimated when extrapolating the data lines of Ti-6Al-4V and copper (Z = 29).

Apart from using data from literature, BSE coefficient can also be estimated by considering Eq. 2 [33].

$$\eta_0 = \frac{7Z - 80}{14Z - 80} \tag{2}$$

Where

η_0 is the BSE coefficient at an incident angle of 0°, and Z is the atomic number of the target material.

A BSE coefficient of 0.36 is obtained when Z is set to 26 for iron with Eq. 2. Thus it is expected that when electronic imaging is carried out on a stainless steel target at 60 keV gun energy (60 kV accelerating voltage) in the EBM machine, the BSE coefficient would be of the order of 0.3, when considering both the data from literature and the estimation from Eq. 2.

2.3 SE yield estimation

Secondary Electrons (SE) yield is the ratio of SE current to the primary electron current. Fig. 6 in the article by Reimer et al [31] shows that when imaging a stainless steel target (represented by iron, Z=26) at a beam energy of 20 keV, the SE yield is 0.2 $\pm$ 0.1. Fig. 7 in the same article [31] shows that when imaging a stainless steel target at 30 keV, the SE yield is also expected to be 0.2 $\pm$ 0.1 (estimated to be between Si, Z=14 and Ag, Z=47).

Although the beam energy range and data resolution of Figs. 6 and 7 in the article by Reimer et al [31] is limited, the trend of SE yield against an increasing beam energy (thus accelerating voltage) can be estimated by the investigation of: (1) the SE escape-depth (Eq. 3 [34]); (2) electron beam penetration-range (Eq. 4 [35]); and (3) the SE yield equation (Eq. 5 [26]), with the use of parameters summarised in Table 3 and a beam energy of 60 keV (accelerating voltage of 60 kV).

Table 3 Properties of iron

Property	Value
Atomic number, Z	26 [36]
Atomic mass, A (amu)	56 [36]
Density, ρ (gcm^{-3})	7.9 [37]
First ionisation energy, I (eV)	7.9 [38]

$$x_s = \frac{2.67 \times 10^{-4} AI}{\rho Z^{\frac{2}{3}}} \qquad (3)$$

Where

X$_s$ (μm) is the SE escape-depth, A (amu) is the atomic mass, I (eV) is the first ionisation energy, ρ is the density (gcm^{-3}).

$$R = \frac{(0.0276 A E^{1.67})}{\rho Z^{0.89}} \qquad (4)$$

Where

R(μm) is the primary electron penetration-range into the target material, E (keV) is the primary electron energy, and Z is the atomic mass of the target material.

$$\delta_0 \propto \frac{1}{E} \qquad \text{for } R \gg X_s \qquad (5)$$

Where

δ$_0$ is the SE yield at an incident angle of 0°.

A SE escape-depth of 1.7 nm and an electron penetration-range of 10 μm are obtained when applying Eqs. 3 and 4. These results indicate that, at an electron beam accelerating voltage of 60 kV (electron energy of 60 keV), the primary beam penetration-range into a stainless steel target is 5882 times the SE escape-depth. Eq. 5 implies that, when the penetration-range is far greater than the escape-depth, the SE yield decreases with increasing primary electron energy (thus its accelerating voltage). Based on these estimations and Figs. 6 and 7 in the article by Reimer et al [31], it is expected that, when electronic imaging is carried out on a

stainless steel target at 60 kV gun accelerating voltage in the EBM machine, the SE yield is less than 0.2.

2.4 Large-area imaging and surface-tilt image contrast simulation

Table 1 shows that the imaging area in the EBM machine is about 40 times greater than that in a typical SEM. Literature shows that, the incident angle between the electron beam and its imaging target leads to surface-tilt contrast in the electronic image [39]. This section describes the computer simulation (Python, open-source) used for the investigation of the surface-tilt image contrast when electronic imaging is conducted in the EBM machine across a stainless steel imaging target. Fig. 1 illustrates the simulation setup; Eq. 6 defines the beam incident angle across a digital electronic image; Eq. 7 [40] and Eq. 8 give the normalised SE yield and BSE coefficient variations with a varying incident angle. Eq. 8 is obtained from generalising Archard's model [41], in order to include any incident angles which are greater than 0. The full derivation of Eq. 8 is given in Appendix A. Table 4 summarises the input parameters of the simulation.
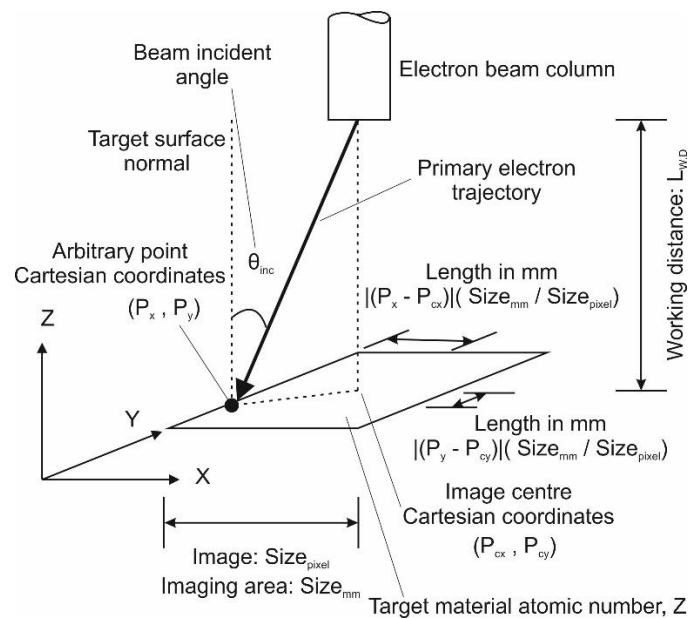

Fig. 1 Surface-tilt image contrast simulation setup

$$\theta_{inc} = \tan^{-1}\left(\frac{\sqrt{(P_x - P_{cx})^2 + \left(P_y - P_{cy}\right)^2}}{L_{W.D}} \frac{Size_{mm}}{Size_{pixel}}\right) \qquad (6)$$

Where

θ_{inc} (degree) is the beam incident angle, $L_{W.D}$ (mm) is the working distance, $Size_{mm}$ (mm) is the width of the imaging area, $Size_{pixel}$ (pixel) is the width of the image, (P_{cx}, P_{cy}) is the image centre Cartesian coordinate of the image, and (P_x, P_y) is the arbitrary point Cartesian coordinate in the image.

$$\frac{\delta_{(\theta_{inc})}}{\delta_0} = \frac{1}{\cos\theta_{inc}} \qquad (7)$$

Where

$\delta_{(\theta inc)}$ is the SE yield at any incident angles, δ_0 is the SE yield at an incident angle of $0°$ (a value of 0.2 is used based on the finding in Section 2.3).

$$\frac{\eta_{(\theta_{inc})}}{\eta_0} = \frac{91 - 20(1 + \cos\theta_{inc})}{51} \qquad (8)$$

Where

$\eta_{(\theta inc)}$ is the BSE coefficient at any incident angles, η_0 is the BSE coefficient at an incident angle of $0°$ (a value of 0.3 is used based on the finding in Section 2.2).

Table 4 Surface-tilt image contrast simulation parameters (a square imaging area and image)

Parameter	Value
Machine beam current (mA)	1
SE yield at incident angle of 0°, δ_0	0.2
BSE coefficient at incident angle of 0°, η_0	0.3
Working distance, $L_{W.D}$ (mm)	400
Image size, $Size_{mm}$ (mm)	180
Image size, $Size_{pixel}$ (pixel)	1800
Image centre coordinates, P_{cx} , P_{cy} (pixel)	(900, 900)
Image coordinate range, P_x , P_y (pixel)	(0-1799, 0-1799)
Pixel colour depth (bit)	8 (256 levels)

2.5 Electronic imaging experimental setup

Fig. 2 (a) is the schematic of the electronic imaging system [14] used in this study. The system consists of a feedback electron sensor (modified Arcam heat-shield frame and plates), a data logger (Arduino DUE microcontroller break-out board), signal amplifier and electronic image generation software. The system is designed to interface with the EBM machine to generate digital electronic images from the feedback electrons, SE and BSE. These feedback electrons are emitted from the interactions between the machine primary electron beam and the processing area/ imaging target. Fig. 2 (b) shows the imaging target used in this study, which is a 210 mm x 210 mm x 5mm (W x D x t) stainless steel plate (Merseyside Metal, UK). The imaging target was bead-blasted manually in a Formula 1200 blasting system (Guyson, UK), with 60 to 80 grit aluminium oxide abrasive to smooth out any uneven surface texture. During electronic imaging, the EBM machine and imaging system were configured according to Table 5. Two sets of electronic imaging experiments were conducted at room temperature, one with helium gas in the machine chamber and the other without. The same

imaging target plate was used in both experiments, and the plate was free from any manual handling when switching between experiments.
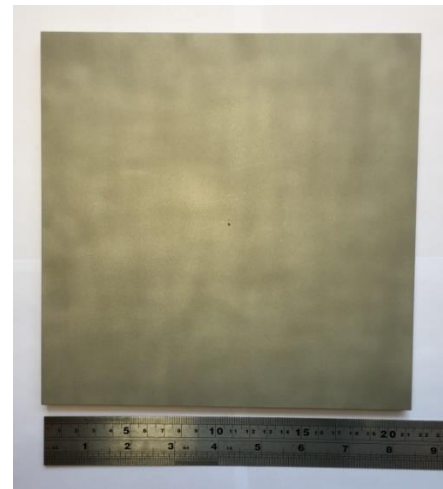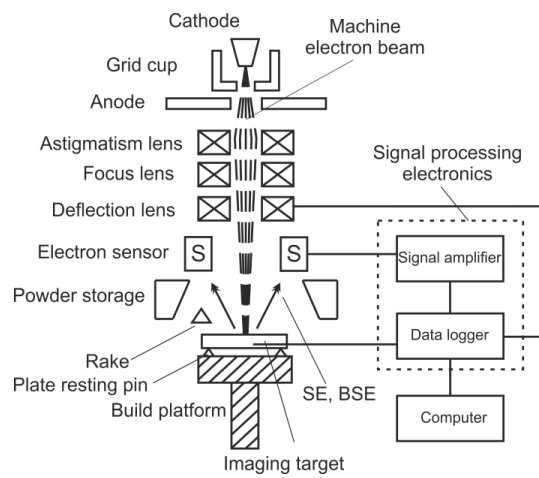
<table>
<tr><td>(a) Schematic of the imaging system [14]</td><td>(b) Imaging target</td></tr>
</table>

Fig. 2 Electronic imaging experimental setup

Table 5 Experimental configuration

Parameter	Value
Imaging System	
Feedback electron sensor bias-voltage	0 V (ground)
Data-logger sampling frequency	118.8 kHz
Image frame time	27.3 s
Current-voltage conversion resistance	1 kΩ
Signal amplifier voltage gain	10
Image size	1800 x 1800 pixels
Image pixel colour depth	8-bit, 256
EBM Machine	
Beam scan / imaging area	180 mm x 180mm
Chamber pressure	2×10^{-3} mbar (with helium)
	2×10^{-5} mbar (without helium)
Beam current	1 mA
Beam speed	11880 mms^{-1}
Beam focus offset	0 mA

3. Results

3.1 Surface-tilt image contrast simulation

Fig. 3 gives the variation in feedback electron signal against the beam incident angle across the EBM machine processing area. The signal is normalised via dividing the signal with an incident angle greater than 0° by the signal at an incident angle of 0° (when the beam hits the centre of the processing area).
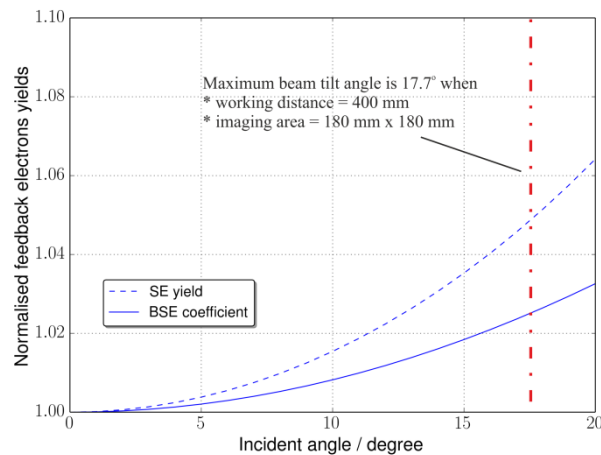

Fig. 3 Normalised feedback electron signal variation
across the EBM machine processing area

Fig. 3 shows that the maximum beam incident angle is 17.7° across a 180 mm x 180 mm area in the EBM processing chamber with a beam working distance of 400 mm. Moreover, it shows that the maximum total variation of feedback electron signals (SE and BSE) is less than 10%. Figs. 4 (a) to (d) are plots with a virtual time scale being the X axis (unit: pixel). The virtual time axis imitates the time-series plot of feedback electron signal during electronic imaging. During typical electronic imaging, the beam raster-scan horizontally from left to right across the top of the imaging target, then moves down to the next scan-line and scans horizontally from left to right again. This beam-scanning motion carries on until the whole region-of-interest is covered. If an oscilloscope is interfaced to the feedback electronic signal data-logger, it would show the electron signal strength (Y axis) against time (X axis). In Figs. 4 (a) to (d), the virtual time scale is pieced together in the following way: the first image pixel row being followed by the second pixel row, and so on, until the whole image frame is shown. Fig. 4 (a) illustrates the trend in beam incident angle with a zoomed-in view by inspecting two image pixel rows (1800 pixel in each row). When moving along a

pixel row (horizontal direction, left to right), the angle decreases and reaches a local minimum when the pixel location hits the Y centreline of the image (central vertical line). Fig. 4 (b) zooms out and shows a bigger picture. The linear variation of the incident angle lower-bound represents the angle variation along the Y centreline of the image, whilst the parabolic upper-bound represents the angle variation along a set of horizontal image pixel rows, moving from the top pixel row to the bottom pixel row of the image. Figs. 4 (c) and (d) illustrate that the estimated normalised BSE and SE yield variations follow the trend of the incident angle, which is expected from Eqs. 7 and 8. Figs. 4 (e) and (f) demonstrate visually the variations in BSE coefficient and SE yield – a top view looking down onto the EBM processing area from above. These simulated bitmaps were set to be 8-bit in pixel colour depth (256 greyscale levels), as given in Table 4, and both show a concentric pattern. Nevertheless, these two greyscale bitmaps are exaggerations of the reality, as they are generated with the < 10% feedback electrons signal variation occupying the whole greyscale range of 256 levels, i.e. the minimum normalised BSE coefficient in Fig. 4 (c) and SE yield in Fig. 4 (d) were assigned a pixel value of 0 (black), whilst the maximum BSE coefficient and SE yield were assigned a value of 255 (white).
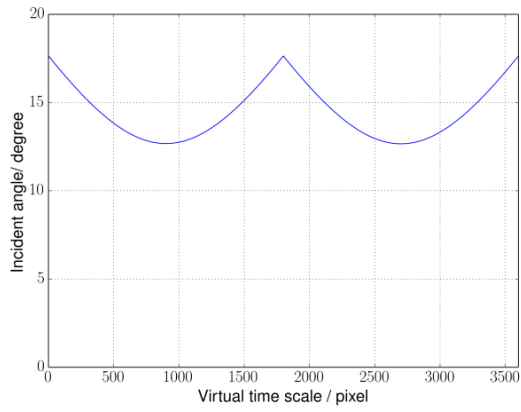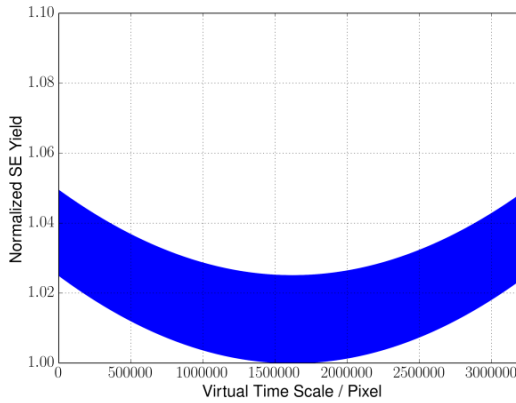
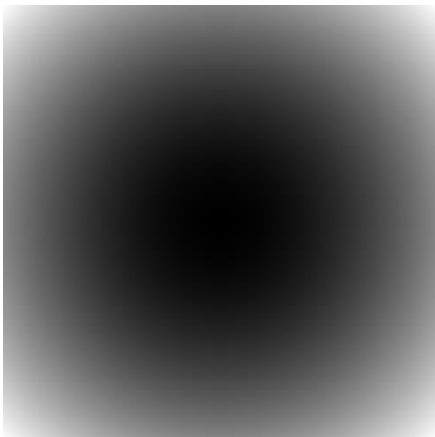(a) Incident angle variation in two pixel rows (1800 pixel / row)
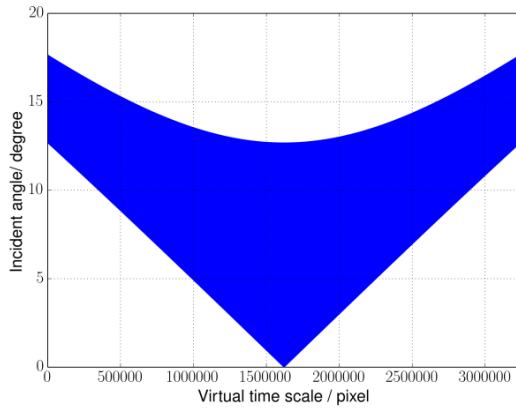
(b) Incident angle variation across an image (1800 x 1800 pixels)
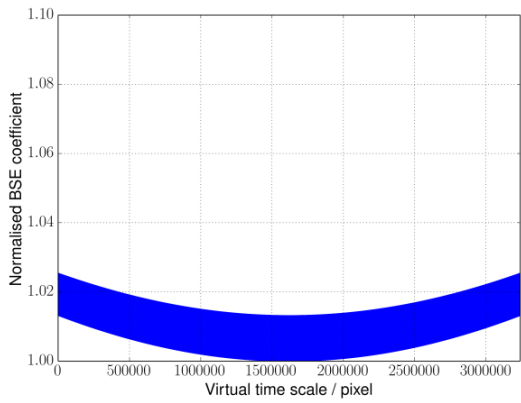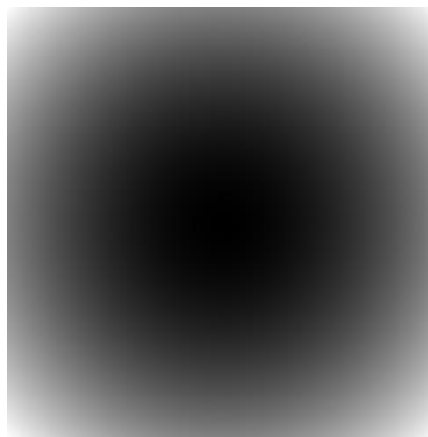

(c) BSE coefficient across an image

(d) SE yield across an image

(e) 8-bit, 2D visualisation of BSE coefficient variation

(f) 8-bit, 2D visualisation of SE yield variation

Fig. 4 Surface-tilt image contrast simulation results

Unlike Figs. 4 (e) and (f), which show the normalised BSE coefficient and SE yield, Fig. 5 shows the actual predicted emission variation across the whole image with 0.5 mA being the total feedback electrons signal at an incident angle of 0° (as machine beam current is 1 mA, δ_0 is 0.2, and η_0 is 0.3, as given in Table 4).
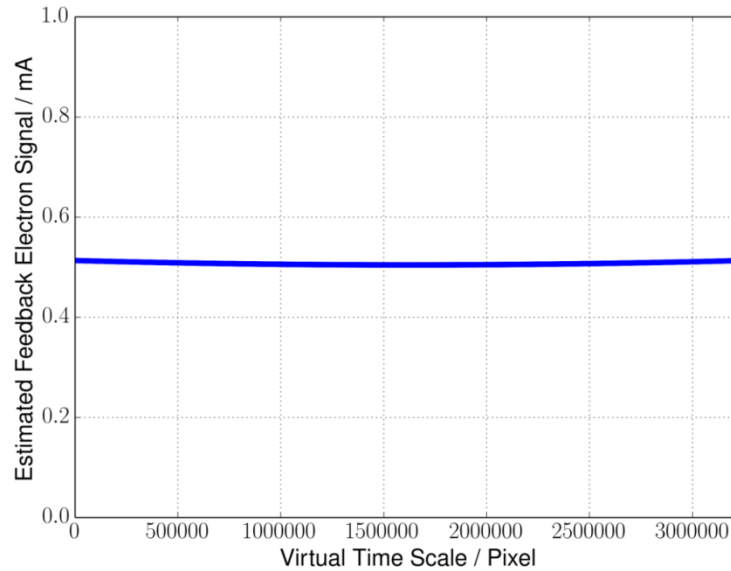

Fig. 5 Total feedback electrons emissions (BSE and SE) variation due to incident angle, across an imaging area of 180 mm x 180 mm, represented in a 1800 x1800 pixels image

Fig. 5 indicates that the maximum signal variation occurs at the top and bottom of the image, where incident angle is at its maximum. Fig. 5 indicates that the maximum level of variation is less than 0.05 mA across the whole image.

3.2 Electronic imaging experiment

Image processing was carried out on the images generated from experiment with the FIJI software (ImageJ, open source). A median filter (Eq. 9 [42]) was employed to remove noise, and histogram equalisation (Eq. 10 [42]) was used to increase image contrast. The median filter applied had a neighbourhood area of a circle with radius of two pixels. The histogram equalisation was carried out with a saturated pixel value of 0.3%.

$$\hat{f}(x,y) = \underset{(s,t)\in S_{xy}}{median}\{g(s,t)\} \tag{9}$$

Where

$\hat{f}$ (x,y) is the pixel-value of the filtered image at (x,y), g(s,t) is the pixel-value of the raw image at (s,t), and S_{xy} represents the set of coordinates within a user-defined area of an image.

$$y_k \triangleq \left| \left[(L-1)\sum_{i=0}^{k} h(i) \right] + 0.5 \right| \qquad k = 0,1,2,\dots\dots,L-1 \tag{10}$$

Where

L is the pixel colour depth (greyscale range) in an image, k is the pixel-value within the greyscale range, L, h(i) is the normalised histogram which gives the probability of occurrence of pixel-value, I, $\sum_{i=0}^{k} h(i)$ is the cumulative probability distribution of the normalised histogram, and y_k is an integer, the equalised number of pixel with a pixel-value of k.

Figs. 6 (a) and (b) show the typical processed electronic images of the stainless steel imaging target. Figs. 6 (c) and (d) are the typical amplified feedback signal time-series plots captured from one image frame. Differences in image contrast can be observed between Fig. 6 (a) and (b), and also when comparing Fig. 6 (c) with (d), when the helium gas was / was not present.
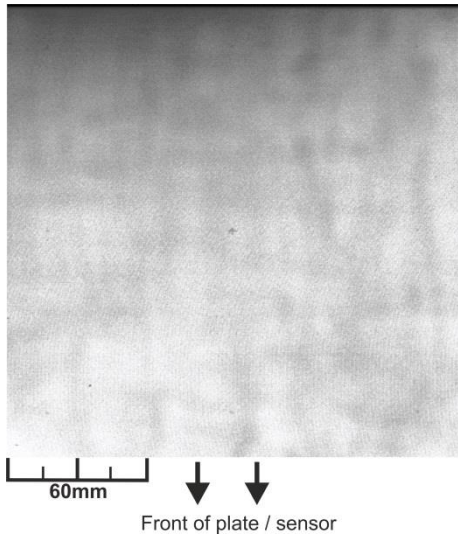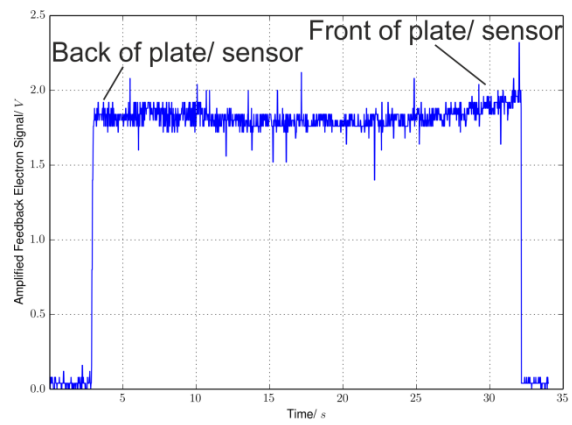
(a) Processed image, no helium gas
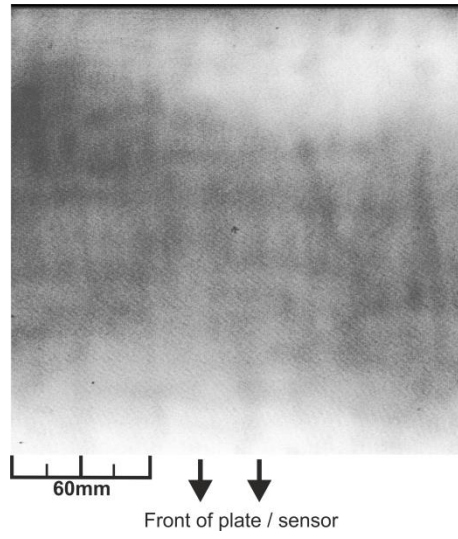
(b) Processed image, with helium gas
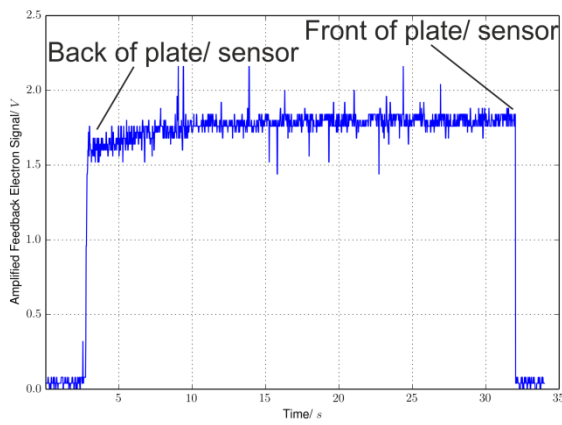
(c) Signal time-series, no helium gas

(d) Signal time-series, with helium gas

Fig. 6 Electronic imaging experimental results

4. Discussion

4.1 Surface-tilt image contrast simulation results

Fig. 4 (b) shows how the incident angle between the machine electron beam and the imaging target varies across a digital electronic image (minimum angle at the image centre, when beam fires directly downwards from the electron gun). Eqs. 7 and 8 show that the BSE coefficient and SE yield are dependent of the incident angle, thus these feedback electron signals also vary across the whole image. The exaggerated simulation results shown in Figs. 4 (e) and (f) indicate that the variation (normalised electron signal, in percentage) is expected to manifest itself in a concentric, circular pattern with a varying image contrast. Nevertheless, Fig. 8 shows that, when estimating the actual signal variation (absolute electron signal, in mA), the difference between the actual signal maximum and minimum is less than 0.05 mA. As a result, the conclusion drawn from the simulation results is that, despite surface-tilt image contrast is expected due to the variation in the beam incident angle, its influence is insignificant and should not create any observable patterns in an electronic image generated from the EBM machine processing area.

4.2 Electronic imaging experimental results

The feedback electron signal level will be discussed first. This will be followed by the observation on surface-tilt image contrast and the influence of the presence of gas in the machine chamber.

Regarding the feedback electron signal level, Section 2.2 and 2.3 predict the BSE coefficient being 0.3 whilst SE yield being 0.2, for an electron beam at 60 kV accelerating voltage, and a stainless steel plate being the imaging target. Table 5 gives the experiment configuration. With beam current being 1 mA and total feedback electron yield estimated to be 0.5 (BSE and SE), the expected raw signal in electric current would be 0.5 mA. As the loading resistance, i.e. the resistance used for current-voltage conversion, is 1 kΩ, and signal amplification gain is 10, the expected amplified signal, which goes into the data-logger would be 5 V. Nevertheless, the average amplified signal observed experimentally was less than 2 V, as shown in Figs. 6 (c) and (d). It is thought that the difference is partly due to the over-estimation of the SE yield. The estimated SE yield of 0.2 given in Section 2.3 is an upper-bound, as this is the SE yield at electron beam energy of 30 keV, as shown in Fig. 6 from the

article by Reimer et al [31]. Eq. 5 shows that SE yield is inversely proportional to the electron beam energy. As a result, the SE yield at an electron gun energy of 60 keV (accelerating voltage of 60 kV) is expected to be much lower than 0.2. In addition, the feedback electron sensor used in this study was a modified Arcam A1 EBM heat-shield frame and plates (Section 2.5), and the sensor surface did not fully encapsulate the processing area. The sensor could not capture all the BSE and SE emitted from the imaging target during electronic imaging.

Regarding the effect of surface-tilt image contrast, the experimental result verifies that the effect is not observable, as predicted by the simulation in Section 3.1, and discussed in Section 4.1. Figs. 6 (a) and (b) show no circular, concentric patterns. Nevertheless, variation in image contrast can be observed in these two figures. It is believed that two main factors contribute to this variation. Firstly, the manual bead-blasting during preparation of the imaging target is thought to have caused non-uniformity in surface texture, leading to a variation in contrast across the imaging target plate. Secondly, the presence of helium gas is thought to have amplified the feedback electron signals at certain locations.

Regarding the effect of the presence of chamber gas, Fig. 6 (a) was generated when the EBM machine helium gas supply was switched off. It shows a different contrast variation pattern when compared with that in Fig. 6 (b), which is an image generated with the presence of helium gas. When the gas is not present, Fig. 6 (c) shows that a delay in the delivery of electron beam current causes the feedback signal to ramp up from 1.5 ± 0.25 V to 1.75 ± 0.25 V from 2.5 ± 2.5 s to 15 ± 2.5 s. On the contrary, when the gas is present, Fig. 6 (d) shows that the ramp-up stage has disappeared and there is an increase in feedback signal towards the end of the image frame, between 25 ± 2.5 s to 32.5 ± 2.5 s. It is postulated that, due to the design of the electron sensor and the location of the EBM machine turbo pump inlets, as shown in Figs. 7 (a) and (b), there is a higher concentration of gas at locations close to the front and rear of the sensor.
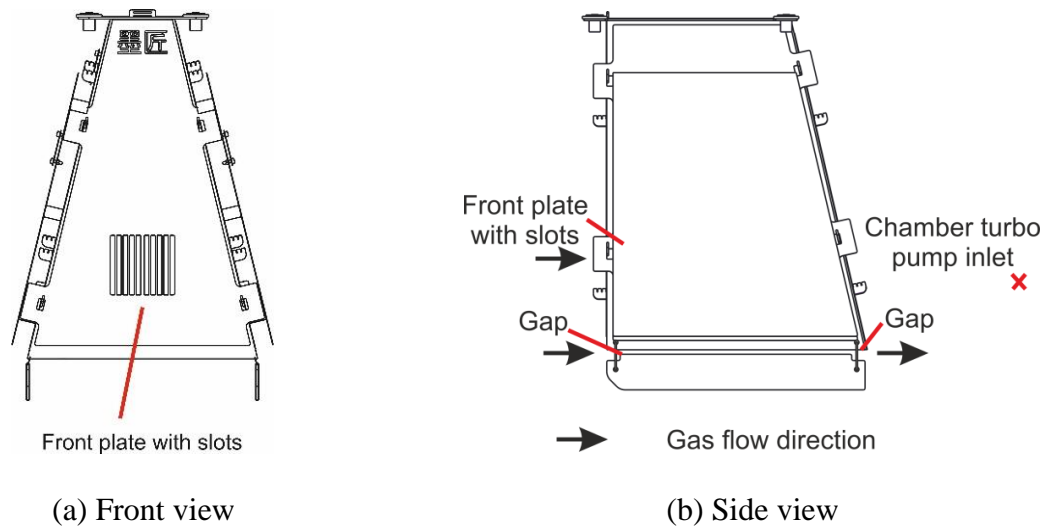
(a) Front view   (b) Side view

Fig. 7 Electron sensor design and the postulated gas flow direction

As introduced in Section 2.1, the presence of gas amplifies the production of feedback electrons due to electrons-gas ionisation events, as depicted in Fig. 8. Fig. 8 shows that the ionised gas molecules accelerate towards either the electron beam or the surface of the imaging target where the beam strikes. SE and BSE are emitted from the target surface due to interactions between the beam and the target. The positively charged gas molecules are attracted to these feedback electrons in order to be neutralised [43]. In addition, although an electrically conductive stainless steel plate was used in the experiment, the plate only sat on resting pins in the chamber processing area without proper grounding, as shown in Fig. 2 (a). Therefore, the discharge of negative charges from the plate to ground is expected to have a time delay due to non-ideal electrical conductivity. During this discharge period, the stainless steel plate behaves like an insulator. Similar to imaging an insulator in LVSEM, negative charges accumulated on the insulator surface attract the positive ionised gas molecules present in the chamber [43]. It is also postulated that, with higher local concentration of gas in the front and the rear of the sensor, the feedback electron signal is amplified at these locations during imaging. This phenomenon thus leads to brighter regions at the top (rear of sensor) and bottom (front of sensor) of the imaging target as shown in Fig. 6 (b); and the disappearance of the ramp-up stage at the start, and the increase in signal at end of the image frame, as shown in Fig. 6 (d). This signal amplification due to the presence of gas molecules is expected to be more significant for a real EBM build. It is because imaging will be done on a metallic powder bed which has lower electrical conductivity than solid metal [44]. This leads to the accumulation of negative charges on the powder bed surface. This phenomenon is similar to sample charging in electron microscopy. Charging occurs when there is an

imperfect conducting path for the electrons to flow to ground from the imaging specimen [30]. If EBM is conducted without the presence of gas, this negative-charging phenomenon of the powder bed surface [45] is likely to lead to "smoke events" (sudden scattering of powder) [46]. The presence of gas helps to suppress "smoke events" by offering an additional charge-neutralisation route for the ionised gas molecules [45].
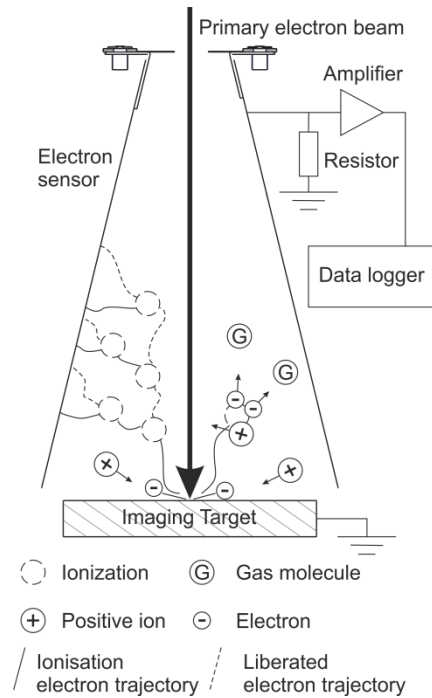

Fig. 8 Gas amplification during electronic imaging

5. Conclusions

In this study, relevant theories and equations are disseminated to benchmark and comprehend the performance of a custom-built electronic imaging system. Analyses and a set of experiments are also presented to address the two challenges when conducting electronic imaging in the EBM machine. These challenges are the surface-tilt image contrast due to large-area imaging, and the gas amplification due to the presence of chamber gas. Prior to experiments, the total feedback electron signal strength was estimated to be at 50% (20% SE and 30% BSE) of the primary electron beam current. In addition, the influence of both the surface-tilt image contrast and the gas amplification were expected to be insignificant based on estimations and simulation results. An electronic imaging experiment was conducted with a custom-built electronic imaging system at room temperature, and the main findings are as follows: (1) the total feedback electron signal strength is of the order of 20%, instead of the estimated 50% of the beam current; (2) there is indeed no observable surface-tilt image

contrast; and (3) contrary to expectation, the gas amplification does create an observable effect in image contrast. This pilot study contributes to the on-going development of an *in-situ* EBM monitoring system. It lays down a foundation to understand the phenomena of surface-tilt and gas amplification when conducting electronic imaging inside an EBM machine. Nevertheless, there are limitations in this pilot study and there will be multiple challenges ahead to realise in-situ electronic imaging, for instance: (1) Data Acquisition (DAQ) rate needs to speed up to meet industrial standards. For instance, DAQ rate shall increase to > 3.24 MHz (26Mbps) to reduce the image frame time to < 1 s (when imaging across an area of 200 mm x 200 mm). This will minimise the additional EBM layer time incurred due to imaging; (2) subsequent investigations into the influence of metallisation (metallic vapour condensation) on image quality and the electron sensor shall be conducted under real EBM condition. During the EBM process, electric charge might accumulate onto the metallic vapour therefore potentially leading to signal saturation when the vapour condenses onto the electron sensor. Moreover, gaps might form between the metallisation thin films and the sensor surface, leading to an increase in the local electrical resistance and inducing undesired local image contrast; and (3) electron sensor design and data-logging circuitry would require modification to cater for an increase in feedback electron signal current during melt-pool imaging. For post-melt raster-scanning imaging, in order to avoid re-melting or surface modification of the processed area, low electron beam current, i.e. 1 mA, shall be used. On the other hand, during melt-pool imaging, instead of raster-scanning the processing area to generate an image, images would be created whilst the electron beam traces the boundary and hatching the interior of a given design cross-section. Typical primary beam current for melting, as well as melt-pool imaging, would be in the range of 3-24 mA [24]. Higher primary beam current leads to greater feedback electron signal current. As a result, the sensor and data-logger need to regulate and limit the signal to avoid damage.

Acknowledgements

References

1. I. Gibson, D.W. Rosen, B Stucker, Additive manufacturing technologies. Springer, New York, pp. 126-128 (2010)

2. X Gong, T Anderson, K Chou, Review on powder-based electron beam additive manufacturing technology. Manufacturing review 1 2. (2014) DOI: 10.1051/mfreview/2014001

3. O.L.A Harrysson, O. Cansizoglu, D.J. Marcellin-Little, D.R Cormier, H.A West, Direct metal fabrication of titanium implants with tailored materials and mechanical properties using electron beam melting technology, Materials science and engineering: C, Volume 28, Issue 3, 2008, Pages 366-373, ISSN 0928-4931 (2008) http://dx.doi.org/10.1016/j.msec.2007.04.022.

4. G. Baudana, S. Biamino, D. Ugues, M. Lombardi, P. Fino, M. Pavese, C. Badini, Titanium aluminides for aerospace and automotive applications processed by electron beam melting: contribution of Politecnico di Torino, metal powder report, Volume 71, Issue 3, 2016, Pages 193-199, ISSN 0026-0657 (2016) http://dx.doi.org/10.1016/j.mprp.2016.02.058.

5. Energetics Incorporated Columbia Maryland. Measurement science roadmap for metal-based additive manufacturing workshop summary report. pages: 61-70, for the National Institute Standard and Technology. U.S Department of Commerce 2013

6. S.B. Tor, C.K. Chua, X. Tan, Y. Kok. Application of electron beam melting (EBM) in additive manufacturing of an impellers. In Proc. of the Intl. Conf. on Progress in Additive Manufacturing (2014)

7. P. Stravroulakis, R.K. Leach, A.T. Clare, S.K. Everton, M. Hirscha. Review of *in-situ* process monitoring and *in-situ* metrology for metal additive manufacturing. Materials and Design, 95:431–445, 2016. DOI: http://dx.doi.org/10.1016/j.matdes.2016.01.099

8. W. J. Sames V. Additive manufacturing of Inconel 718 using electron beam melting: processing, post-processing, & mechanical properties. PhD thesis, Texas A&M University, Nuclear Engineering (2015)

9. M. Mani, B. Lane, A. Donmez, S. Feng, S. Moylan, R. Fesperman, NISTIR 8036. Measurement science needs for real-time control of additive manufacturing powder bed fusion processes (2015). http://dx.doi.org/10.6028/NIST.IR.8036

10. J. Raplee, A. Plotkowski, M.M. Kirka, R. Dinwiddie, A. Okello, R.R. Dehoff, S.S Babu, Thermographic microstructure monitoring in electron beam additive

manufacutirng, Scientific Reports 7, Article Number: 43554 (2017) doi:10.1038/srep43554

11. T. Scharowsky, A. Bauereiß, R.F. Singer, C. Körner, Observation and numerical simulation of melt pool dynamic and beam powder interaction during selective electron beam melting, Proceedings from the solid freeform fabrication symposium, Austin, pp 815–820 (2012)

12. R.B. Dinwiddie, R.R. Dehoff, P.D. Lloyd, L.E. Lowe, J.U.B Ulrich, Thermographic *in-situ* process monitoring of the electron-beam melting technology used in additive manufacturing, Proceeding of SPIE, Thermosense: thermal infrared applications XXXV, 87050K (2013) doi:10.1117/12.2018412

13. S. Price, J. Lydon, K. Cooper, K Chao, Experimental temperature analysis of powder-based electron beam additive manufacturing, Proceedings from the solid freeform fabrication symposium, pp. 162-173 (2013)

14. H. Wong, D. Neary, E. Jones, P. Fox, C. Sutcliffe, Pilot capability evaluation of a feedback electronic imaging system prototype for in-process monitoring in electron beam additive manufacturing, Springer International Journal of Advanced Manufacturing Technology, in-press (2018) DOI: 10.1007/s00170-018-2702-6

15. C. Arnold, C. Pobel, F. Osmanlic, C. Körner, Layerwise monitoring of electron beam melting via backscatter electron detection. Rapid Prototyping Journal 24/8 (2018) 1401–1406. DOI 10.1108/RPJ-02-2018-0034

16. Arcam AB. Arcam A1 EBM Specification. DOI: http://www.arcam.com/wp-content/uploads/Arcam-A1.pdf

17. H. Bruining, Physics and Applications of Secondary Electron Emission, Pergamon Press Ltd, London, 1954, p. 88.

18. H. Wong, D. Neary, E. Jones, P. Fox, C. Sutcliffe (2019) Pilot feedback electronic imaging at elevated temperatures and its potential for in-process electron beam melting monitoring, Elsevier Additive Manufacturing 27 (2019) 185–198, https://doi.org/10.1016/j.addma.2019.02.022

19. L. Reimer. Scanning electron microscopy: Physics of image formation and microanalysis, pages 4–5. Springer (1998) ISBN: 3-540-63976-4.

20. ATI Ti-6Al-4V, Grade 5, Technical data sheet, https://www.atimetals.com/Products/Documents/datasheets/titanium/alloyed/ati_6-4_tds_en_v1.pdf

21. ATI 625™ Nickel-Base Superalloy, Technical data sheet, https://www.atimetals.com/Products/Documents/datasheets/nickel-cobalt/nickel-based/ati_625_ludlum_version_tds_en_v1.pdf

22. J.I. Goldstein, D.E. Newbury, J.R. Michael, N.W.M. Ritchie, J.H.J. Scott, D.C. Joy, Scanning Electron Microscopy and X-Ray Microanalysis, forth edition, Springer, 2018, p. 30.

23. L. Reimer. Scanning electron microscopy: Physics of image formation and microanalysis, pages 13–19. Springer (1998) ISBN: 3-540-63976-4.

24. J. Luft, T. Weißgarber, B. Kieback, A. Kirchner, B. Klöden. Process window for electron beam melting of Ti-6Al-4V. In Euro PM2014 – AM: Technologies Manuscript (2014)

25. J. Ran, Y. Yue, X. Wang, H. Luo. Measurement of the first townsend's ionization coefficients in helium, air, and nitrogen at atmospheric pressure. Journal of the Physical Society of Japan , Vol 83 (2014) https://doi.org/10.7566/JPSJ.83.074503

26. W.G. Trodden, R.O. Jenkins. Electron and ion emission from solids, pages 58–62. London Routledge and Kegan Paul Ltd (1965)

27. L. Reimer. Scanning electron microscopy: physics of image formation and microanalysis, pages 117-120. Springer (1998) ISBN: 3-540-63976-4.

28. I.M. Watt. The principle and practice of electron microscopy, page 162. Cambridge University Press, 1997. ISBN: 9780521435918, http://ebooks.cambridge.org/.

29. A. Gunasekaran. Scanning electron microscopy. course material, LA SIGMA Microscopy workshop, the LONI Institute, https://www.institute.loni.org/lasigma/document_files/workshopdocuments/SEMnotes.pdf.

30. JEOL. SEM scanning electron microscope A to Z: basic knowledge for using the SEM. Pages: 21-26. https://www.jeol.co.jp/en/applications/pdf/sm/sem_atoz_all.pdf

31. C. Tollkamp, L. Reimer. Measuring the backscattering coefficient and secondary electron yield inside a scanning electron microscope. Scanning, 3:35–39 (1980)

32. W.E. Miller. Transmission and backscatter coefficients of 1.0- to 3.0-mev electrons incident on some metals and alloys. NASA Technical Note NASA TN D-5724 (1970) https://ntrs.nasa.gov/archive/nasa/casi.ntrs.nasa.gov/19700016194.pdf

33. D.J. Stokes. Principle and practice of variable pressure environmental scanning electron microscopy (VP-ESEM), pages 64–120. Wiley, A John Wiley and Sons, Ltd, Publication (2008) ISBN: 978-0-470-06540-2.

34. K. Kanaya, S. Ono. The energy dependence of secondary emission based on the range-energy retardation power formula. J. Phys. D: Appl. Phys.,, 12:619–632 (1979) (http://iopscience.iop.org/0022-3727/12/4/019).

35. S. Okayama, K. Kanaya. Penetration and energy-loss theory of electrons in solid targets. Journal of Physics D: Applied Physics, 5-43:43–58 (1972)

36. M. E. Wieser, N. Holden, T. B. Coplen, Pure, Atomic weights of the elements (IUPAC Technical Report)Appl. Chem., Vol. 85, No. 5, pp. 1047–1078 (2013) http://dx.doi.org/10.1351/PAC-REP-13-03-02

37. H. E. Cleaves, J. M. Hiegel, Properties of high-purity iron, Journal of research of the national bureau of standards, Volume 28, U. S department of commerce (1942)

38. Chem 130 course materials: structure and properties of inorganic compounds, Depauw University (2018), http://dpuadweb.depauw.edu/harvey_web/Chem130/PDF_Files/Handouts/consecutive IonizationEnergy.pdf

39. L. Reimer. Scanning electron microscopy: physics of image formation and microanalysis, pages 222–224. Springer (1998) ISBN: 3-540-63976-4.

40. R.F. Egerton. Physical principles of electron microscopy, page 132. Springer (2005)

41. G.D. Archard. Back scattering of electrons. Journal of Applied Physics, 32:573–585 (1961) DOI: http://dx.doi.org/10.1063/1.1728385

42. R.E. Woods, R.C. Gonzalez. Digital image processing, pages 122–127, 322–327. Pearson Education, Inc. (2008)

43. M. Toth, B.L. Thiel, A.M. Donald, Interpretation of secondary electron images obtained using a low vacuum SEM, Ultramicroscopy 94 (2003) 71–87, DOI: https://doi.org/10.1016/S0304-3991(02)00203-6

44. J.M. Montes, F.G. Cuevas, J. Cintas, J.M. Gallardo, Electrical conductivity of metal powder aggregates and sintered compacts, J Mater Sci (2016) 51:822–835, DOI: 10.1007/s10853-015-9405-2

45. P. Cordero, J. Mireles, S. Ridwan et al. Evaluation of monitoring methods for electron beam melting powder bed fusion additive manufacturing technology. Prog Addit Manuf 2, 1–10 (2017). DOI: https://doi.org/10.1007/s40964-016-0015-6

46. S. Vock, B. Klöden, A. Kirchner, T. Weißgärber, B. Kieback, Powder for powder bed fusion: a review, Progress in Additive Manufacturing (2019) 4:383–397, DOI: https://doi.org/10.1007/s40964-019-00078-6

Appendix A
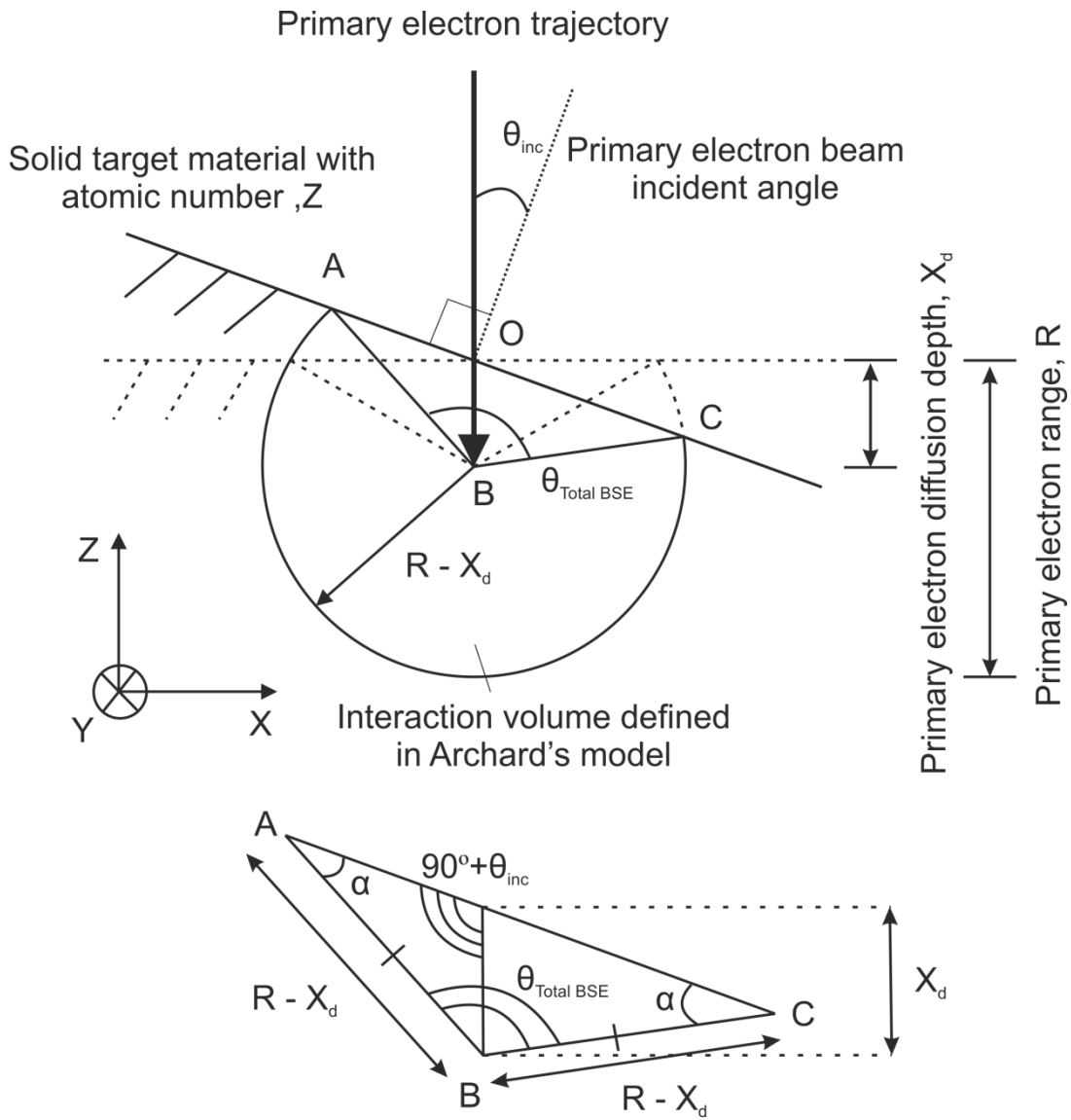
Considering ΔABC and applying the law of sines,

$$\frac{x_d}{\sin \alpha} = \frac{R - x_d}{\sin(90° + \theta_{inc})} \tag{A.1}$$

$$\frac{x_d}{\sin \alpha} = \frac{R - x_d}{\cos \theta_{inc}}$$

$$\sin \alpha = \frac{x_d \cos \theta_{inc}}{R - x_d}$$

From Archard's model on primary electrons penetrating into a solid target [41]

$$\frac{x_d}{R} = \frac{40}{7Z} \tag{A.2}$$

Eq. A.2 into Eq. A.1,

$$\sin \alpha = \frac{\frac{40}{7Z}\cos\theta_{inc}}{1 - \frac{40}{7Z}}$$

$$\alpha = \sin^{-1}\left(\frac{40\cos\theta_{inc}}{7Z - 40}\right) \tag{A.3}$$

From the diagram, ΔABC is an isosceles triangle,

$$\theta_{Total\ BSE} = 180° - 2\alpha$$

$$\theta_{Total\ BSE} = 180° - 2\sin^{-1}\left(\frac{40\cos\theta_{inc}}{7Z - 40}\right)$$

$$\boxed{\theta_{Half\ BSE} = 90° - \sin^{-1}\left(\frac{40\cos\theta_{inc}}{7Z - 40}\right)} \tag{A.4}$$

Archard's model [41] says that the backscattered electron coefficient, $\eta_{(\theta_{inc})}$, at an arbitrary primary electron beam incident angle, θ_{inc}, is given as,

$$\eta_{(\theta_{inc})} = \frac{Solid\ angle\ of\ the\ BSE\ cone}{Solid\ angle\ of\ an\ interaction\ sphere}$$

$$\eta_{(\theta_{inc})} = \frac{2\pi\left(1 - \cos\theta_{Half\ BSE}\right)}{4\pi}$$

$$\eta_{(\theta_{inc})} = \frac{1 - \cos\theta_{Half\ BSE}}{2} \tag{A.5}$$

Eq. A.4 into A.5,

$$\eta_{(\theta_{inc})} = \frac{1 - \cos\left[90° - \sin^{-1}\left(\frac{40\cos\theta_{inc}}{7Z - 40}\right)\right]}{2}$$

$$\eta_{(\theta_{inc})} = \frac{1 - \sin\left[\sin^{-1}\left(\frac{40\cos\theta_{inc}}{7Z - 40}\right)\right]}{2}$$

$$\eta_{(\theta_{inc})} = \frac{1 - \frac{40\cos\theta_{inc}}{7Z - 40}}{2}$$

$$\eta_{(\theta_{inc})} = \frac{1}{2}\left(1 - \frac{40\cos\theta_{inc}}{7Z - 40}\right)$$

$$\boxed{\eta_{(\theta_{inc})} = \frac{7Z - 40(1 + \cos\theta_{inc})}{14Z - 80}} \tag{A.6}$$

Again, according to Archard's model [41], for a special case where the incident angle of a primary electron beam is at $0°$, the backscattered electron coefficient, η_0, is expressed as,

$$\eta_0 = \frac{7Z - 80}{14Z - 80} \tag{A.7}$$

Eq. A.7 can be derived from Eq. A.6 when setting θ_{inc} as 0°. With stainless steel being the target material (iron, Z=26), in order to calculate the normalised BSE coefficient at an arbitrary incident angle, considering both Eq. A6 and A7,

$$\frac{\eta_{(\theta_{inc})}}{\eta_0} = \frac{\dfrac{7Z - 40(1 + \cos\theta_{inc})}{14Z - 80}}{\dfrac{7Z - 80}{14Z - 80}}$$

$$\frac{\eta_{(\theta_{inc})}}{\eta_0} = \frac{91 - 20(1 + \cos\theta_{inc})}{51} \qquad (A.8)$$